RSC Advances

PAPER

View Article Online
View Journal | View Issue

Cite this: *RSC Adv.*, 2022, **12**, 18923

Simultaneous removal of Pb^{2+} and direct red 31 dye from contaminated water using *N*-(2-hydroxyethyl)-2-oxo-2*H*-chromene-3-carboxamide loaded chitosan nanoparticles†

Mehrez E. El-Naggar, *[a] Emad K. Radwan, *[b] Huda R. M. Rashdan, [c] Shaimaa T. El-Wakeel, [b] Asmaa A. Koryam [b] and Ahmed Sabt[d]

This study reports the preparation of a new material that can remove synthetic dyes and trace metals simultaneously. A new coumarin derivative was synthesized and its chemical structure was inferred from spectral data (FT-IR, ^{1}H-NMR, ^{13}C-NMR). Meanwhile, chitosan nanoparticles (CsNPs) were prepared then used as a carrier for two different concentrations of the coumarin derivative (C1@CsNPs and C2@CsNPs). The TEM, SEM and DLS findings illustrated that the prepared nanocomposites exhibited spherical shape and small size (less than 200 nm). The performance of the prepared material for the removal of an anionic dye (direct red 31, DR31) and cationic trace metal (Pb^{2+}) was evaluated in unary and binary systems. The results revealed that complete removal of 10 mg L^{-1} of DR31 and Pb^{2+} in unary system was achieved at pH_o 3.0 and 5.5 using 0.5 and 2.0 g L^{-1}, respectively, of C2@CsNPs. The adsorption of DR31 and Pb^{2+} followed different mechanisms as deduced from the effect of pH_o, kinetic, isotherm and binary adsorption studies. The adsorption of DR31 followed the Langmuir isotherm model and the pseudo-first-order kinetic model. While, the adsorption of Pb^{2+} followed Freundlich isotherm model and Elovich kinetic model. In the binary system, the co-presence of DR31 and Pb^{2+} did not affect the adsorption of each other's. Overall, the prepared material showed promising results for the removal of anionic dyes and cations trace metals from contaminated water.

Received 20th April 2022
Accepted 24th June 2022

DOI: 10.1039/d2ra02526d

rsc.li/rsc-advances

Introduction

Water stress and crisis are growing worldwide as a result of population growth and industrial advancement. The aquatic environment receives large amounts of highly polluted industrial wastewater which deteriorates its quality.[1] Synthetic dyes and trace metals are two prominent groups of contaminants that co-occur in several industrial effluents[2–4] and pose momentous impacts to the human and living things.[1,2,5] Presence of synthetic dyes in the aquatic environment limits the light penetration, and increases the organic load and turbidity thus interrupt the photosynthesis process, reduces the dissolved oxygen and causes toxicity to aquatic flora and fauna.[1,2,6] Moreover, some synthetic dyes are hazardous because of their toxicity, carcinogenicity, mutagenicity, teratogenicity, and stability in the environment for long periods.[1,6–10] On the other side, trace metals are one of the most hazardous contaminants due to their non-biodegradability, bioaccumulation, high mobility and toxicity.[3,5,11,12] Amongst trace metals, lead is widely used in several industries and consequently a common contaminant.[11] Exposure to lead have been linked to cancer, anorexia plumbism, anemia, damage of brain, liver, kidney, and memory and disorder of neuronal, nervous, and reproductive systems.[5,13] Humans and animals are exposed to dyes and heavy metals through ingestion of contaminated water and food.[9,11] Therefore, decontamination of water from synthetic dyes and trace metals is essential to protect the public health.[6,9,13] In this context, several chemical, physical, biological and combined treatment techniques have been applied to remove dyes and trace metals from water.[1,2,4,14,15] Adsorption is one of these techniques that is characterized by high efficiency, cost effectiveness, simplicity, flexibility, ease operation, inertness towards toxic contaminants and eco-friendliness.[2,5,6,10,12,16,17] Therefore, adsorption has gained immense attention as

[a]*Institute of Textile Research and Technology, National Research Centre, 33 El Buhouth St, Dokki, Giza, 12622, Egypt. E-mail: mehrez_chem@yahoo.com*
[b]*Water Pollution Research Department, National Research Centre, 33 El Buhouth St, Dokki, 12622 Giza, Egypt. E-mail: emadk80@gmail.com*
[c]*Chemistry of Natural and Microbial Products Department, Pharmaceutical and Drug Industries Research Institute, National Research Centre, 33 El Buhouth St, Dokki, 12622, Egypt*
[d]*Department of Natural Compounds Chemistry, Pharmaceutical and Drug Industries Research Institute, National Research Centre, 33 El Buhouth St, Dokki, 12622 Giza, Egypt*

† Electronic supplementary information (ESI) available. See https://doi.org/10.1039/d2ra02526d

a promising technology for decontaminating water from toxic dyes and trace metals.[9] Selecting a suitable adsorbent material ensures the success of the adsorption process as the adsorbent rules the affinity to the targeted contaminant and rate of adsorption.[5] Accordingly, research and development to find an economic adsorbent that has high efficiency for the removal of several types of contaminants from water is now required.[17]

Coumarin based compounds and their fused derivatives belong to benzopyrone family and are widespread in nature at different concentrations as active ingredients in several plants and fruits such as cinnamon, vanilla, apricot, strawberry, and cherry.[18–22] They are well known by their sweet herbaceous scent and has a wide range of applications in different industrial sectors such as food, pharmaceuticals, and cosmetics industries.[19,23–25] Also, they are used intensively as sensitizers in the dye sensitized solar cells and fluorescent probe. In addition, they are used as optical brightening agents and laser dyes.[23] Moreover, coumarins exhibited a wide range of therapeutic and biological applications. In this regard, they revealed antioxidant, anticoagulant, anticancer, antimicrobial, antifungal, antidiabetic, antiparasitic, anti-inflammatory and antiviral properties.[26–33] However, there application in water/wastewater treatment is scarce. For example, Nuñez-Dallos *et al.*,[34] reported the preparation of a new coumarin salen ligand that can bind metal ions by the azomethine and phenolic hydroxyl groups of the coumarin moieties. The new coumarin chelating-adsorbent improved the Pb(II) and Cd(II) accumulation step which enhanced the sensitivity of Pb(II) and Cd(II) by anodic stripping voltammetry greatly. More recently, Bhaumick and Choudhury[35] reported the preparation and application of coumarin containing 1,4-polytriazoles for different water-soluble dyes. They reported high adsorption efficiency for methylene blue and attributed this efficiency to the presence of moieties required for π–π, cation–π, and ion–dipole interactions. These studies inspired us to prepare a new coumarin derivative and apply it for contaminated water treatment.

On the other hand, chitosan-based biopolymer has attracted the attention in recent years as a result of their unique chemical features, which enable them to be used in a multitude of applications including medicine, textile, and environment. Due to the presence of amine groups which become protonated at low pH levels, chitosan is converted to a water-soluble cationic polyelectrolyte at pH below 6.0. Crosslinking of chitosan reduces its solubility in acidic medium albeit at the expense of hydroxyl and amino groups.[36] Further enhancement in the characteristics of chitosan can be achieved by converting it into nanoform which results in higher surface area. The utilization of chitosan in industrial wastewater treatment as sorbent agent has received great attention by scientists owing to its coagulating/flocculating features. Thus, as previously reported,[37–39] chitosan was used for removing dyes, pesticides and heavy metals from textile wastewater.

The present study aims to prepare a new material designed to enable the simultaneous removal of two different major groups of pollutants, specifically, anionic synthetic dyes and cationic trace metals. *N*-(2-Hydroxyethyl)-2-oxo-2*H*-chromene-3-carboxamide (compound **4**) was prepared *via* the reaction of coumarin-3-carboxylate (compound **3**) with 2-aminoethanol in the presence of catalytic amount of piperidine under reflux. Meanwhile, CsNPs were prepared *via* ionic gelation process in the presence of sodium tripolyphosphate as crosslinking agent. Then, CsNPs were used as a carrier to encapsulate two different concentrations of compound **4**, nominated as C1@CsNPs and C2@CsNPs depending on the utilized concentration of compound **4**. The structure and features of the prepared materials were evaluated using Fourier transform infrared spectroscopy (FTIR), proton nuclear magnetic resonance (^{1}H-NMR) spectroscopy, carbon-13 nuclear magnetic resonance (^{13}C-NMR) spectroscopy, field emission scanning electron microscope (FE-SEM), high-resolution transmission electron microscopy (HR-TEM) and dynamic light scattering (DLS). The adsorption efficiency of the newly prepared materials toward direct red 31 as an example for anionic dyes and Pb^{2+} as an example of cationic trace metals was assessed. The effect of different experimental conditions such as solution initial pH, material amount, contact time and initial concentration of adsorptive on the adsorption process was investigated in unary system. The adsorption kinetic data was analyzed by the Lagergren pseudo-first-order (PFO), pseudo-second-order (PSO), and Elovich models. While the isotherm data was analyzed by numerous two-parameter (Langmuir, Freundlich, Temkin, Dubinin–Radushkevich (D–R)) and three-parameter (Redlich–Peterson (R–P), and Sips) models to find the best suited one. The simultaneous removal of DR31 and Pb^{2+} was investigated and the McKay and Al Duri model was applied to explore the mutual effect of the coexistence of DR31 and Pb^{2+} on their adsorption. Finally, the adsorption was confirmed and a mechanism was proposed based on the results of structural and adsorption analysis.

Materials and methods

Chemicals

The chemicals used for the preparation and the instruments used to characterize the prepared materials are given in the ESI.†

Preparation of *N*-(2-hydroxyethyl)-2-oxo-2*H*-chromene-3-carboxamide (compound 4). A mixture of salicylaldehyde (4.880 g, 40 mmol), diethyl malonate (7.200 g, 45 mmol), catalytic amount of piperidine (0.5 mL) and 2–3 drops of acetic acid were dissolved in 25 mL of absolute ethanol. The mixture refluxed for 2 h. After cooling to RT, the solution was slowly poured into ice-water. Ethyl 2-oxo-2*H*-chromene-3-carboxylate (compound **3**, m.p. 96–98 °C) was filtrated, collected, recrystallized from ethanol and separated as white crystals (51% yield). Then, a mixture of ethyl 2-oxo-2*H*-chromene-3-carboxylate (2.185 g, 10 mmol), and 2-aminoethanol (0.613 g, 10 mmol) were dissolved in 25 mL absolute ethanol. The mixture was submitted to reflux for 38 h. After the reaction was ended, the solvent was evaporated, a yellow solid was precipitated, collected, and purified by column chromatography using ethyl acetate/petroleum ether (1 : 2, v/v) as eluent to get compound **4** as white powder (45% yield). 179–181 °C. ^{1}H-NMR (DMSO d_6, 500 MHz) δ (ppm): 9.15 (s, 1H, NH), 8.90 (s, 1H, ArCH

= C), 7.27–7.35 (m, 2H, ArH), 7.37–7.40 (2H, ArH), 3.83 (t, 2H, CH_2), 3.62 (q, 2H, CH_2), 3.13 (s, 1H, OH); ^{13}C-NMR (DMSO d_6, 100 MHz): δ: 162.8, 161.3, 154.4, 148.6, 134.1, 129.8, 125.3, 118.5, 118.0, 116.6, 62.4, 42.9.

Preparation of compound 4 loaded chitosan nanoparticles. Accurate weight (1.0 g) of chitosan (Cs) was dispersed in 1% glacial acetic acid and kept under mechanical stirring at ambient temperature for 60 min. Meanwhile, 1.5 g of sodium tripolyphosphate (STPP) was dissolved in 100 mL of distilled water. On the other hand, 1 g of compound **4** was dissolved in 50 mL of acetic acid at 50 °C with the aid of magnetic stirring for 15 min. After the complete dissolution of all compounds, solutions of STPP (crosslinking agent) and compound **4** were gradually added to Cs solution and held under continuous mechanical stirring for another 60 min. During the addition of STPP solution, the chitosan solution was turned to milky color due the STPP crosslinking effect. After 60 min, the produced solution was centrifuged at 10 000 rpm for 1 h and the resultant wet powders were dried in a vacuum oven for 1 h at 120 °C to get compound **4** loaded chitosan nanoparticles with two different concentrations. The accurate volumes of the components used in the formulation of nanocomposites are listed in Table 1.

Adsorption performance evaluation. Different phases of batch mode adsorption studies were carried out in this work. First, the adsorption performance of the different prepared materials was investigated and compared. Then the effects of adsorptive solution initial pH (pH_o), mass of material and contact time on the adsorption efficiency of the best performing material was evaluated. Afterword, the adsorption kinetics and isotherm were evaluated. These phases were performed in a single component system. In the last phase, the simultaneous adsorption of dye and trace metal in a two-component system was evaluated. All experiments were performed in triplicate at room temperature using an orbital shaker set at 350 rpm. Direct red 31 (DR31, also known as direct red 12B) dye which is an anionic double azo direct dye was used as a model for dyes. Fig. S1a† displays the structure and digital photograph of the dye solution. The concentration of DR31 was determined using JASCO V730 (Japan) UV-vis spectrophotometer. The visible spectra of the different concentration of DR31 and the calibration curve are shown in Fig. S1b and c,† respectively. Fig. S1b† reveals that the maximum wavelength of DR31 is 522 nm and Fig. S1c† exposes the excellent linearity of the calibration curve over the concentration range 0–100 mg L^{-1}. For trace metals, lead was used as model and its concentration was determined using inductively coupled plasma optical emission spectrometer (ICP-OES, Agilent 5100). The adsorption performance was evaluated in terms of percentage removal or amount adsorbed per gram of material. The ESI† provide full details about the analysis of the adsorption data.

Table 1 Volume of each component for the preparation of CsNPs and C@CsNPs nanocomposites

Sample code	Chitosan solution (mL)	STPP solution (mL)	Compound **4** solution (mL)
CsNPs	50	30	—
C1@CsNPs	50	30	5
C2@CsNPs	50	30	15

Results and discussion

Ethyl 2-oxo-2*H*-chromene-3-carboxylate **3** was synthesized by stirring of salicylaldehyde and diethylmalonate in ethanol containing catalytic amount of piperidine according to Knoevenagel condensation.[40] Then, coumarin-3-carboxylate **3** was refluxed with 2-aminoethanol in presence of catalytic amount of piperidine to afford the desired amide-containing coumarin based derivative *N*-(2-hydroxyethyl)-2-oxo-2*H*-chromene-3-carboxamide **4** as shown in Scheme 1. Its chemical structure was studied and demonstrated by its spectral data. The ^{1}H-NMR spectrum showed singlet signal at 9.15 ppm for NH, singlet signal at 8.90 ppm for Ar CH=C, triplet signal at 3.83 for CH_2 and quartet signal at 3.62 ppm for CH_2. Finally, it revealed a singlet signal at 3.13 ppm for OH group. The ^{13}C-NMR spectrum exhibited significant signals at 162.8 and 161.3 for (C=O), 154.4 for (C=C–O), 148.6, 134.1, 129.8, 125.3, 118.5, 118.0, 116.6, and 62.4 for (CH_2), and 42.9 for (CH_2) (Fig. 1). The FTIR spectrum (Fig. 3) revealed strong absorption bands at 3382 cm^{-1} and 3322 cm^{-1} indicating the presence of OH and NH groups, respectively. The two strong absorption bands at 1699 cm^{-1} and 1639 cm^{-1} are for the two carbonyl groups. These results demonstrate the successful preparation of compound **4**.

Fig. 2 a, b and c presents the surface morphology of the prepared CsNPs, C1@CsNPs and C2@CsNPs, respectively. It can be noted that CsNPs exhibit approximately spherical shape with a particle size in nanometric scale. These particles are agglomerated in large clusters with rough surface. After CsNPs loading with different concentrations of compound **4**, the morphological features were changed. Fig. 2b and c shows that compound **4** was deposited on the rough surface of CsNPs leading to decreasing the surface roughness. Fig. 2b shows that the surface of sample C1@CsNPs has many bumps indicating the partial filling of the valleys on the surface of CsNPs by compound **4**. Increasing the concentration of compound **4** (sample C2@CsNPs) results in nearly smooth surface indicating the complete filling of the valleys on the surface of CsNPs. The deposition of compound **4** onto the surface of CsNPs leads to the formation of nanocomposite with large particles. And the particle size increases as the concentration of compound **4** increases, C2@CsNPs has larger particle size than C1@CsNPs. This observation will be further verified by DLS analysis.

For further illustration about the particle shape of CsNPs, C1@CsNPs and C2@CsNPs, HRTEM analysis was utilized. The HRTEM image of CsNPs (Fig. 2d), reveals that they are distinct particles having spherical shapes. The physical appearance of CsNPs was changed after loading with compound **4**. As shown in Fig. 2e and f the observed individual particles of C1@CsNPs and C2@CsNPs, respectively, exhibited two colors; faint and deep black colors. The faint color can be attributed to compound **4** that is deposited onto the surface of CsNPs and the deep color can be attributed to the CsNPs itself.

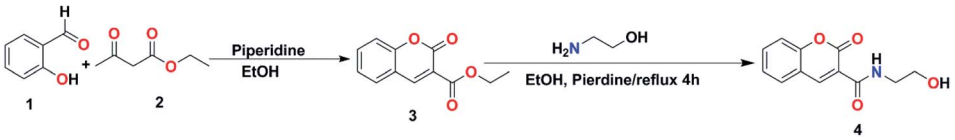

Scheme 1 Synthesis of *N*-(2-hydroxyethyl)-2-oxo-2*H*-chromene-3-carboxamide (compound **4**).

In order to determine the average particles size of the prepared samples, DLS was performed. Fig. 2g depicts the hydrodynamic size of CsNPs, C1@CsNPs and C2@CsNPs. It can be seen that the average size of CsNPs, C1@CsNPs and C2@CsNPs is 106, 122 and 185 nm, respectively. Additionally, the polydispersity index (PDI) is 0.124, 0.146 and 0.223 for CsNPs, C1@CsNPs and C2@CsNPs, respectively. As noted from DLS, the particle size of these nanoparticles is greater than that of TEM and SEM. This phenomenon can be ascribed to the difference in the utilized measuring techniques. In DLS technique, the samples are dispersed in water and held in the instrument for about 18 runs. During the time of runs, the nanoparticles tend to swelled and causing enlargement in the size of the evaluated nanoparticles. In addition, the movement of the particles in the aqueous solvent results in collision and ultimately leads to the formation of clusters or agglomerated particles. On contrary, for TEM evaluation, the samples were well dispersed in water and immediately placed on the TEM grids for solvent evaporation. Overall, the DLS results further support the observation that increasing the loading of compound **4** results in increasing the particle size. By checking the PDI of the three samples, the values are less than 0.5 implying that the nanoparticles are formed with homogeneous features.

FTIR spectra was used to examine the surface functional groups of CsNPs, C1@CsNPs and C2@CsNPs (Fig. 3). As previously described by Samuels,[41] an amine deformation peak at 1605 cm^{-1} and an amide I carbonyl stretch at 1643 cm^{-1} have been shown in pure chitosan. The peak 1258 cm^{-1} that indicated the P=O group of STPP[42] emerged in the spectra of the C@CsNPs nanocomposites.

The amine deformation peak shifted from 1605 cm^{-1} to 1540 cm^{-1}, and the peak at 1558 cm^{-1} evolved into a strong peak, implying that an interaction was taking place at the amine group of CsNPs, which might indicate tripolyphosphate interaction. Moving to the FTIR of compound **4**, it can be observed that there are many peaks exhibited at 3382, 3322, 1699, 1639 and 1603 cm^{-1}. The peaks at 3382 cm^{-1} and 3322 cm^{-1} can be attributed to the presence of OH and NH groups, respectively. The strong absorption band at ν 1699 cm^{-1} can be ascribed to the carbonyl group of the side chain while the strong absorption band at ν 1639 cm^{-1} can be assigned to the carbonyl group of the coumarin ring. Finally, the presence of a signal at 1603 cm^{-1} can be assigned for C=C. The sample C2@CsNPs was selected as representative for the evaluation of the FTIR spectra of C@CsNPs nanocomposites. It is remarkable that, most of the intensity of the peaks of compound **4** were reduced or totally disappeared which could be attributed to its low concentration percentage relative to CsNPs.

The sample C2@CsNPs was selected to evaluate the roughness properties before and after the simultaneous adsorption of DR31 and Pb^{2+}. The amplitude roughness average increased from 34.7 nm to 41.1 nm after the adsorption process. The increase in the value of roughness average refers to the change in the nature of surface roughness from smooth homogenous surface to uppermost roughness surface after the adsorption process. Fig. 4 further clarify this observation. On the other hand, the value of maximum height of the roughness parameters (391.5 and 370.8 nm before and after the adsorption process, respectively) shows the low indication in the deep surface roughness after the adsorption process. Also, the values of maximum roughness valley depth (189.1 and 188.2 nm before and after the adsorption process, respectively) and the maximum roughness peak heights (202.4 and 182.6 nm before and after the adsorption process, respectively) confirm that the influence of change in roughness of C2@CsNPs surface.

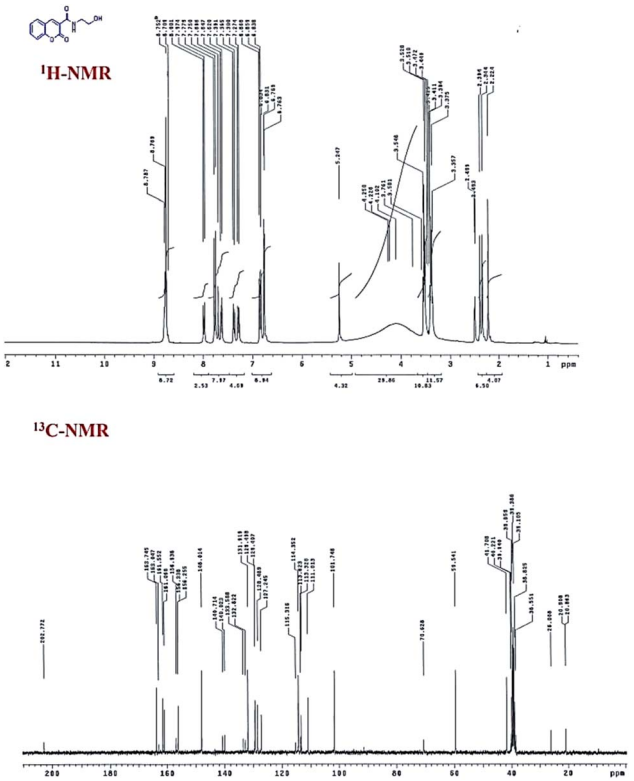

Fig. 1 ^{1}H-NMR and ^{13}C-NMR spectra of compound **4**.

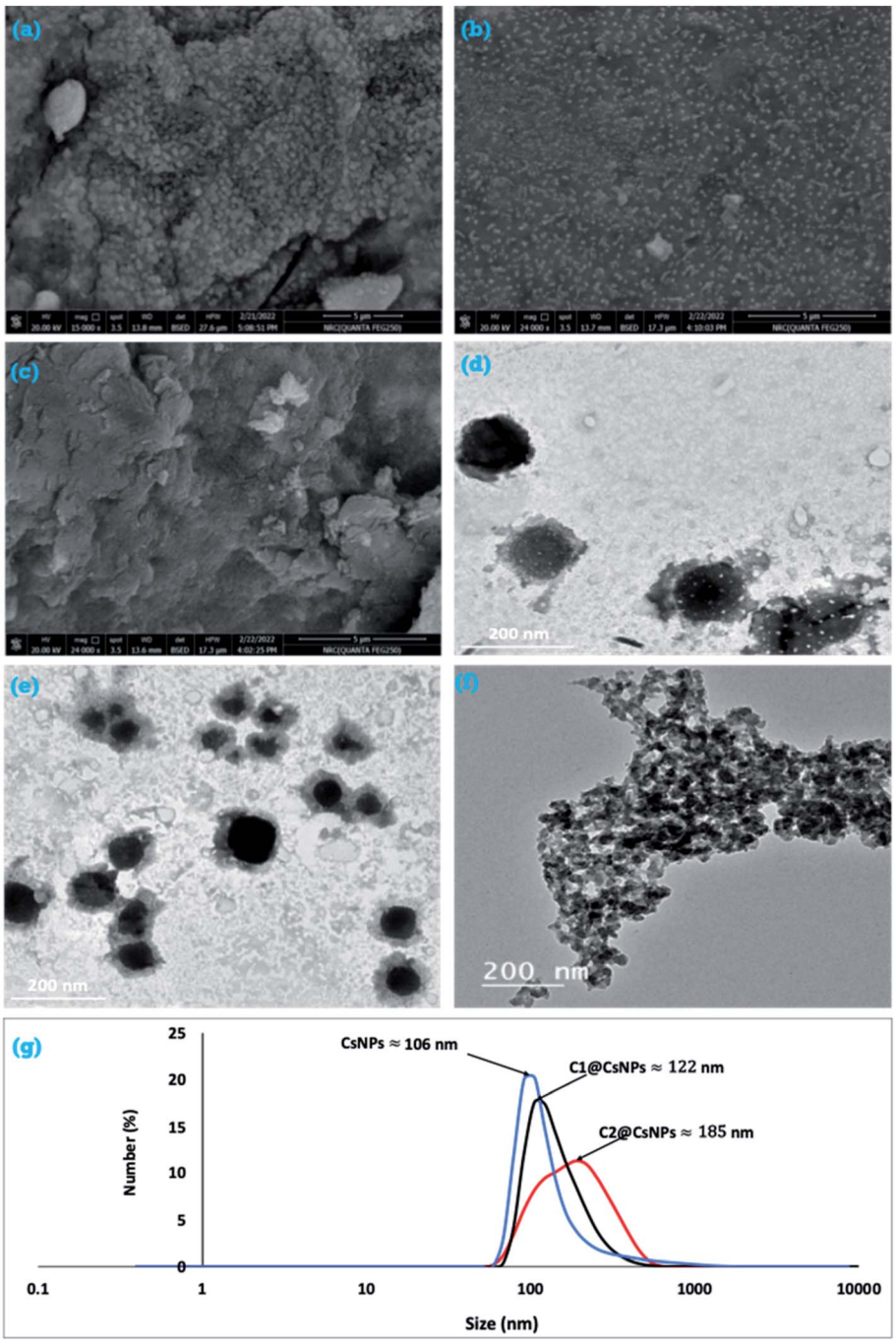

Fig. 2 FESEM (a, b and c), HRTEM (d, e and f) and DLS (g) of CsNPs, C1@CsNPs and C2@CsNPs, respectively.

Adsorption performance study

As illustrated above, chitosan has $-NH_2$ and –OH groups while compound **4** has –CONH, –OH, –C═O and phenyl groups. The C@CsNPs composite is expected to combine these functional groups, thus, increase the number of potential adsorption sites. These functional groups can drive the adsorption of DR31 *via* electrostatic interactions, hydrogen bonding, n–π interactions, and/or π–π interactions.[43–45] While for Pb^{2+}, electrostatic interactions, complexation and/or surface precipitation can drive the adsorption process.[46]

Comparing the efficiency of the prepared materials. The adsorption performance of all prepared materials towards DR31 and Pb^{2+} was evaluated by contacting 50 mg and 100 mg of each material with 50 mL of 10 mg L^{-1} of DR31 and Pb^{2+}, respectively, at the spontaneous pH_o of the adsorptive solution (5.3 for DR31 and 5.5 for Pb^{2+}) in a single component system. Fig. 5 displays the results.

A significant increase in DR31 removal (from 74% to 83%) can be observed by modifying CsNPs with compound **4** (sample C1@CsNPs) as shown in Fig. 5a. This result agrees with

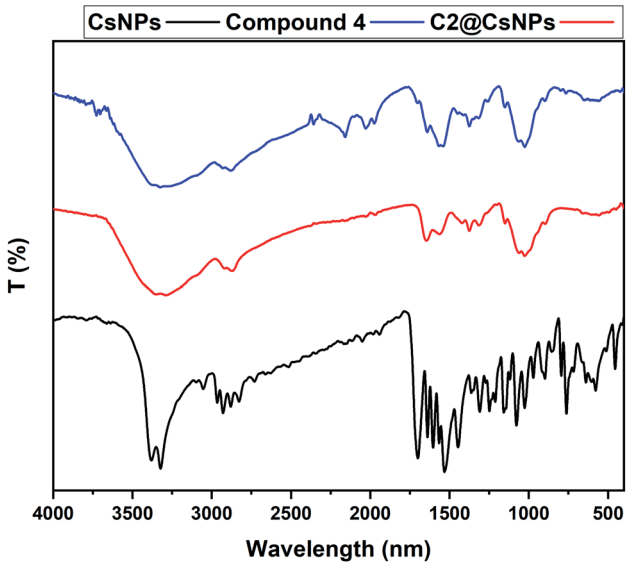

Fig. 3 FTIR of compound **4**, CsNPs and C2@CsNPs.

increasing the potential adsorption sites by the addition of compound **4**. Further increase in the amount of compound **4** (sample C2@CsNPs) has insignificant effect on DR31 removal ($R\% = 82$). Which is likely due to hiding some adsorption sites of CsNPs by the added compound **4**. Another probable reason is the hiding of some adsorption sites of compound **4** due to its agglomeration when higher concentration was used.

On the other side, Fig. 5b shows that the sample C1@CsNPs has a slightly higher adsorption affinity toward Pb^{2+} than CsNPs (after 2 h the $R\%$ changed from 89% to 94%). Which indicates that the added functional groups have minor role in the adsorption process probably due to their unavailability as adsorption sites as a result of resonance or protonation effects. Further increase in the amount of compound **4** loaded onto CsNPs (sample C2@CsNPs) produced a slight decrease in $R\%$ to 82%. A probable reason is the blocking of some adsorption sites of CsNPs by the added compound **4**.

Remarkably that the adsorption of both DR13 and Pb^{2+} by all prepared materials has a stepwise nature, *i.e.* the percentage of adsorptive removed increases gradually with contact time. Overall, the sample C1@CsNPs can be considered as the best performing material for both DR13 and Pb^{2+} and will be used henceforward.

Effect of adsorption parameters

Initial pH (pH_o) of adsorptive solution. pH_o of the adsorptive solution is a central parameter that affects the adsorption process and provides important data about the adsorption mechanism. pH_o controls (i) the surface charge of the adsorbent by controlling the dissociation/protonation of the surface functional groups, (ii) the charge of dye by controlling the dissociation/protonation of the functional groups of the dye, and (iii) the speciation degree of hydration of trace metal.[5,8,11,13] Dependance of the adsorption process on the pH_o infers that electrostatic interactions and/or complexation mechanism are effective.[46] In this study, the effect of pH_o on the adsorption performance was investigated in a single component system at room temperature in the pH_o range 3.0–9.0 for DR31 and 2.0–5.5 for Pb^{2+}. The initial concentration for both adsorptive was 10 mg L^{-1} and the dosage was 0.5 g L^{-1} for DR31 and 2.0 g L^{-1} for Pb^{2+}. The results are given in Fig. 6a and b.

Fig. 6a indicates that changing the pH_o over the range 5.3 to 9.0 has insignificant effect on the $R\%$ of DR31. Over the pH_o range 5.3 to 9.0, about 64% of DR31 was removed after 2 h. Increasing the DR31 solution pH_o to 3.0 caused a drastic increase in $R\%$ to 96%. The structure of DR31 (Fig. S1a†) contains two sulphonate groups attached to two naphthalene rings. These sulphonate groups are strong electrolytes that dissociate entirely in water rendering DR31 a negative charge in solution.[47] Under acidic conditions the functional groups of the adsorbent become protonated and attract the negatively charged DR31 dye. Thus, the electrostatic attractions between the anionic groups of DR31 and the cationic functional groups of the adsorbent (resulting from protonation) play key role in the adsorption process under acidic conditions. Increasing the solution acidity ensures the complete protonation of all functional groups and consequent higher removal of DR31 dye. So, the highest removal was observed at pH_o 3. Several studies have reported maximum adsorption for anionic dyes at acidic pH.[15,47–50] Under neutral and alkaline conditions, the functional groups of C1@CsNPs become either neutral or deprotonated. Thus, electrostatic attractions disappear, consequently, the $R\%$ of DR31 decreases. However, DR31 still adsorbed which suggests the involvement of adsorption mechanism(s) other than electrostatic attractions. So, one or more of π–π stacking between the benzene ring of C1@CsNPs and the aromatic backbone of DR31, hydrogen bonding between the hydroxyl groups on C1@CsNPs and nitrogen and oxygen atoms in DR31 (dipole–dipole H-bonding), hydrogen bonding between the

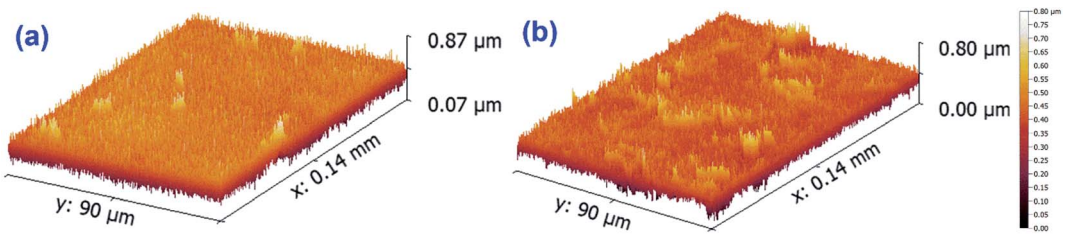

Fig. 4 Roughness properties of C2@CsNPs, (a) before and (b) after DR31 and Pb^{2+} adsorption.

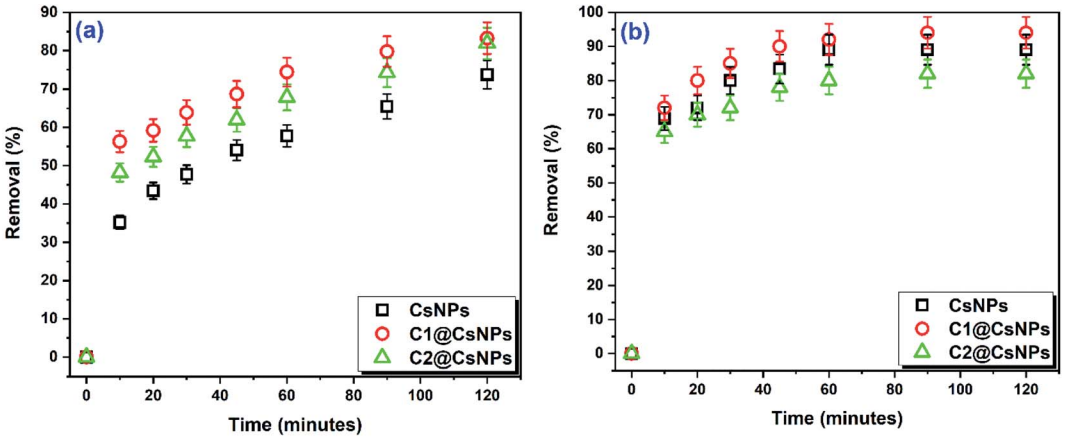

Fig. 5 Effect of compound 4 concentration on the removal of (a) DR31 dye (pH_o 5.3, C_o 10 mg L^{-1}, dosage 1.00 g L^{-1}) and (b) Pb^{2+} (pH_o 5.5, C_o 10 mg L^{-1}, dosage 2.00 g L^{-1}) as a function of contact time.

hydroxyl groups on C1@CsNPs and the aromatic rings in DR31 (Yoshida H-bonding), interactions between the oxygen atoms in C1@CsNPs and aromatic rings of DR31 (n–π interactions), interactions between the sulphonate groups and the aromatic rings of C1@CsNPs (anion–π interactions) might trigger the adsorption process under neutral and alkaline conditions.[43–45,51]

Contrarily, Fig. 6b indicates that the adsorption of Pb^{2+} was lowest at highly acidic solution (pH_o 2, $R = 40\%$) and increases with decreasing the acidity of solution reaching the highest

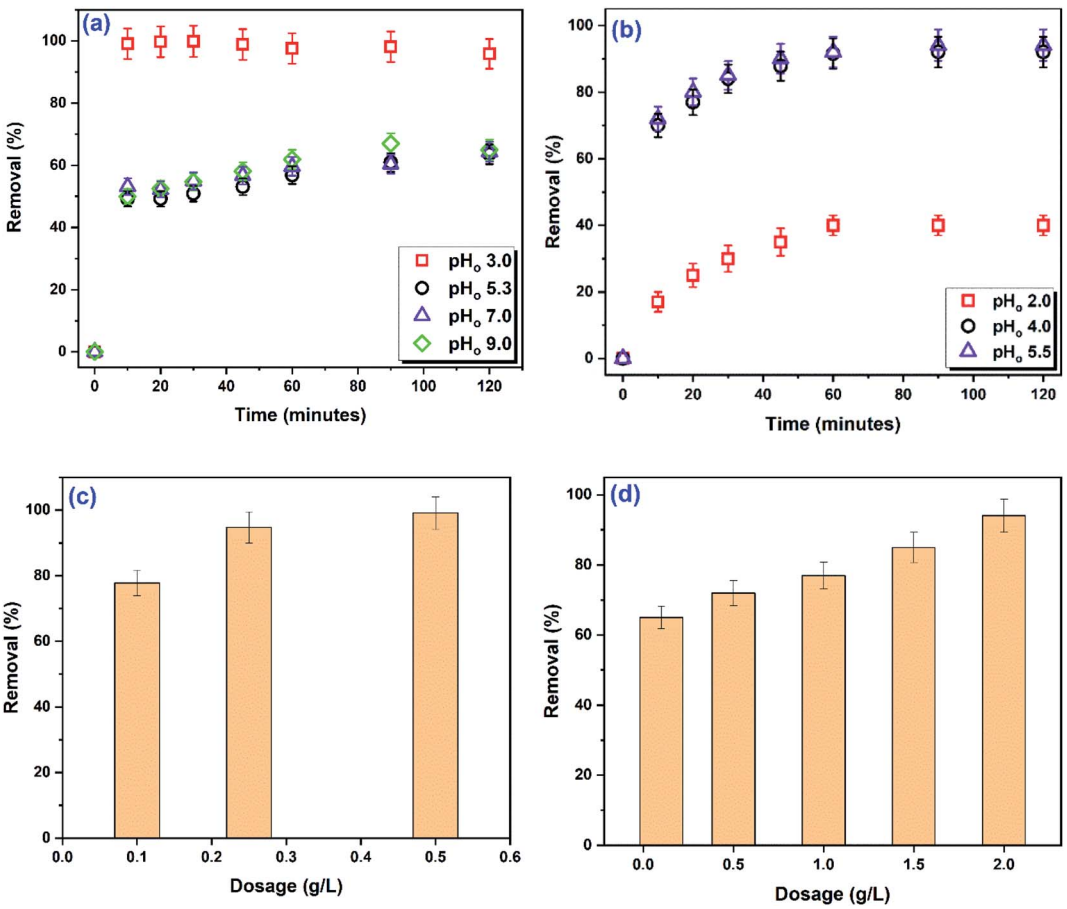

Fig. 6 Time-course change of *R*% as a function of pH_o, (a) DR31 dye (C_o 10 mg L^{-1}, dosage 0.50 g L^{-1}) and (b) Pb^{2+} (C_o 10 mg L^{-1}, dosage 2.00 g L^{-1}); change of *R*% as a function of C1@CsNPs amount, (c) DR31 dye (pH_o 3, C_o 10 mg L^{-1}, contact time 30 min) and (d) Pb^{2+} (pH_o 5.5, C_o 10 mg L^{-1}, contact time 90 min).

value (92%) at pH_o 4. Further decrease in the acidity of solution to pH_o 5.5 did not translate to significant increase in the adsorption of Pb^{2+} ($R = 94\%$). At highly acidic conditions, the H^+/H_3O^+ dominates the competition with Pb^{2+} for the adsorption sites on the surface of C1@CsNPs causing an electrostatic repulsion between the protonated functional groups and Pb^{2+} which results in decreasing the adsorption percentage. As the solution acidity decreases the protonation of the functional groups of C1@CsNPs decreases consequently the electrostatic forces changes from repulsion to attraction owing to the presence of lone pair of electrons on functional groups such as $-NH_2$ and –OH. These lone pair of electrons can also be donated to Pb^{2+} forming a complex.[46] Thus, it seems that electrostatic interactions and metal ion complexation are the chief mechanisms governing the adsorption of Pb^{2+} onto C1@CsNPs. This behaviour has been frequently reported before.[13,16,17,46,52] Overall, the pH_o has a substantial influence on the adsorption of both DR31 and Pb^{2+} onto C1@CsNPs. Further experiments were executed at pH_o 3.0 for DR31 and 5.5 for Pb^{2+}.

Contact time. Over the pH_o range 5.3–9.0, a high R% of DR31 was achieved at the first 10 minutes then the R% gradually increased continuously (Fig. 6a). Similar trend can be observed for Pb^{2+} over the studied pH_o range (Fig. 6b). The high R% in the first 10 minutes is owing to the availability of large number of vacant adsorption sites. The decelerating in the increasing of R% rate is a result of the occupation of adsorption sites and attaining their saturation (equilibrium state). Such behavior is common in the literature.[5,9,11,17] Notably that the adsorption of DR31 at pH_o 3 was quite fast and attained the equilibrium in 10 minutes. While for Pb^{2+} the equilibrium time was 90 minutes.

Mass of adsorbent. To investigate the effect of C1@CsNPs amount on the adsorption process, different amounts of C1@CsNPs were suspended in 50 mL of 10 mg L^{-1} of adsorptive solution preadjusted to pH_o 3.0 and 5.5 for DR31 and Pb^{2+}, respectively, in a single component system. Samples were withdrawn from Pb^{2+} solution after 90 minutes and from DR31 solution after 30 minutes. The R% was calculated and graphed *vs.* the C1@CsNPs amount as shown in Fig. 6c and d. Even little amount of C1@CsNPs achieves a good removal of DR31, as displayed in Fig. 6c, 0.10 g L^{-1} of C1@CsNPs can remove 78% of DR31. Increasing the amount of C1@CsNPs to 0.25 g L^{-1} brings about a significant increase in DR31 removal percentage to 95%. A trivial increase in R% to 99% was achieved by increasing the amount of C1@CsNPs to 0.50 g L^{-1}. On the other hand, Fig. 6d shows that the amount of Pb^{2+} removed increases continuously and significantly with increasing the amount of C1@CsNPs reaching 94% at 2.00 g L^{-1} of C1@CsNPs. Generally, increasing R% with the adsorbent amount is ascribed to increasing the number of adsorption sites.[13,53] While the non-increase in R% in spite of increasing the adsorbent amount is commonly ascribed to the agglomeration of the adsorbent and consequent inaccessibility to adsorption sites or approaching the complete removal of the adsorptive.[54,55]

Kinetics. To get information about the adsorption mechanism, the kinetic data was analyzed by the Lagergren pseudo-first-order (PFO), pseudo-second-order (PSO), and Elovich models. The non-linear forms of these models, coefficient of determination (R^2) and error values (chi-square (χ^2) and root-mean-square deviation (RMSD)) are given in the ESI.† Non-linear fitting of the experimental data to these models is displayed in Fig. S2† and the estimated parameters of the kinetic models, R^2 and error values are listed in Table 2. The values of R^2 suggest that all the studied kinetics models fit the experimental data of DR31 dye well. However, both PFO and PSO are better fitted to the data than Elovich model. The values of error functions further evinced this observation since PFO and PSO have lower error values than Elovich model. Also, analysis of R^2, error values and comparing the q_e calculated from the model to the experimental one (18.81 mg g^{-1}) indicate that both PFO and PSO have very close values and that PFO fits the experimental data slightly better than PSO. Moreover, the value of k_2 of PSO and α of Elovich models look unrealistic. Wang and Ariyanto[56] reported similar behavior for the adsorption of malachite green on natural zeolite. They found that both PFO and PSO fit good the experimental data and the PFO gives q_e value much closer to the experimental one. Therefore, they concluded that the adsorption process follows the PFO kinetics. Likewise Pishnamazi *et al.*,[9] reported that both PFO and PSO can represent the kinetics of the adsorption of acid orange II and acid fuchsin dyes on multifunctionalized nano-silica KCC-1 and that the PFO has slightly higher adjusted R^2. They concluded that both of the PFO and PSO models can predict the adsorption process however the PFO model is more suitable to model the adsorption kinetics. Also, several reports found that the PFO gives the best fit to the experimental data.[15,57–61]

For Pb^{2+} adsorption, Table 2 shows that Elovich model has the highest R^2 and lowest error values indicating that the adsorption kinetics can be accurately described by Elovich model. Thus, according to Elovich assumptions, the adsorption of Pb^{2+} onto C1@CsNPs follows a chemisorption process involving surface chelation, electron-transfer, and/or sharing/

Table 2 Kinetic parameters for DR31 and Pb^{2+} adsorption onto C1@CsNPs

	Direct red 31 dye	Pb^{2+}
PFO model		
R^2	0.9986	0.9508
χ^2	0.06	0.08
RMSE	0.25	0.28
q_e	18.82 ± 0.01	3.84 ± 0.10
k_1	1.01 ± 0.45	0.27 ± 0.05
PSO model		
R^2	0.9985	0.9857
χ^2	0.07	0.02
RMSE	0.26	0.15
q_e	18.81 ± 0.11	4.07 ± 0.07
k_2	$1.00 \times 10^{43} \pm 2.63 \times 10^{44}$	0.12 ± 0.02
Elovich model		
R^2	0.9967	0.9967
χ^2	0.149	0.01
RMSE	0.386	0.07
α	$1.55 \times 10^{43} \pm 5.43 \times 10^{44}$	694.78 ± 451.32
β	5.56 ± 1.93	3.01 ± 0.19

exchange of electrons between C1@CsNPs and Pb^{2+}. It also indicates that the surface of C1@CsNPs has energetically heterogeneous adsorption sites. Previously, several studies reported the good fitting of Elovich to the adsorption of trace metals on different adsorbents.[13,62,63]

Isotherm. Isotherm study was conducted to get more details about the adsorption mechanism and nature of the adsorbent. Also, mathematical modeling of the adsorption isotherms provides essential data for the design and field application of adsorption system. The adsorption isotherm experiments were performed using 0.50 and 2.00 g L^{-1} of C1@CsNPs at pH 3.0 and 5.5 using 10–100 and 25–300 mg L^{-1} initial concentration for DR31 and Pb^{2+}, respectively. The contact time was extended to 1 h and 2 h for DR31 and Pb^{2+}, respectively, to ensure sufficient time for reaching equilibrium state. The experimental isotherm was analyzed by two- and three-parameter models, specifically, Langmuir, Freundlich, Temkin, Dubinin–Radushkevich (D–R), Redlich–Peterson (R–P), and Sips models. Details about these models are given in the ESI.† The plots of the experimental isotherm and fitting curves of the different isotherm models are displayed in Fig. S3.† The corresponding extracted parameters of the isotherm models as well as the R^2 and error values are compiled in Table 3.

Analyzing the values of R^2 and error functions (Table 3) reveals that, for DR31, Langmuir has the highest R^2 and lowest error values among the different investigated two-parameter models. Extending the comparison to the three-parameter isotherm models disclose that both Sips and Langmuir have equal R^2 that is lower than R–P model. Further comparison of the error values indicates that Langmuir is the best model that

Table 3 Isotherm parameters for DR31 and Pb^{2+} adsorption onto C1@CsNPs

Direct red 31 dye							
Two-parameter isotherm models							
Freundlich		Langmuir		Temkin		D–R	
R^2	0.9214	R^2	0.9869	R^2	0.9501	R^2	0.9769
χ^2	43.07	χ^2	7.19	χ^2	27.33	χ^2	12.63
RMSE	6.56	RMSE	2.68	RMSE	5.23	RMSE	3.55
K_F	33.93 ± 3.82	q_L	58.13 ± 1.40	b_T	345.88 ± 54.00	q_{D-R}	55.30 ± 1.57
n	6.82 ± 1.63	K_L	1.35 ± 0.21	A_T	90.63 ± 96.86	K_{D-R}	0.13 ± 0.02
Three-parameter isotherm models							
R–P				Sips			
R^2		0.9874		R^2		0.9869	
χ^2		8.29		χ^2		8.62	
RMSE		2.88		RMSE		2.94	
K_{R-P}		83.72 ± 19.46		q_S		57.96 ± 2.24	
a		1.51 ± 0.50		K_S		1.37 ± 0.29	
g		0.99 ± 0.03		n_S		1.02 ± 0.24	
Pb^{2+}							
Two-parameter isotherm models							
Freundlich		Langmuir		Temkin		D–R	
R^2	0.9984	R^2	0.9953	R^2	0.9678	R^2	0.8865
χ^2	1.49	χ^2	4.31	χ^2	29.50	χ^2	103.88
RMSE	1.22	RMSE	2.08	RMSE	5.43	RMSE	10.19
K_F	4.04 ± 0.35	q_L	102.80 ± 7.26	b_T	136.61 ± 15.15	q_{D-R}	61.95 ± 7.77
n	1.77 ± 0.06	K_L	0.01 ± 0.00	A_T	0.22 ± 0.06	K_{D-R}	86.45 ± 44.95
Three-parameter isotherm models							
R–P				Sips			
R^2		0.9996		R^2		−0.0917	
χ^2		0.44		χ^2		1332.37	
RMSE		0.66		RMSE		36.50	
K_{R-P}		2.86 ± 0.71		q_S		19.59 ± 26.77	
a		0.27 ± 0.15		K_S		$0.04 \pm 1.88 \times 10^{12}$	
g		0.60 ± 0.05		n_S		$17.52 \pm 3.30 \times 10^{13}$	

Table 4 Langmuir monolayer saturation capacity for DR31 and Pb^{2+} by several adsorbents

DR31				Pb^{2+}			
Adsorbent	q_L (mg g^{-1})	$C_{o,max}$ (mg L^{-1})	pH_o	Adsorbent	q_L (mg g^{-1})	$C_{o,max}$ (mg L^{-1})	pH_o
This work	58.13	100	3.0	3-Aminopropyltriethoxysilane modified cellulose acetate[65]	185.36	200	5.0
Zinc ferrite NPs modified by cetyl trimethylammonium bromide[66]	55.56	200	7.0	This work	102.80	300	5.5
$ZnCl_2$ activated *Jatropha* husk carbon[67]	39	50	2.0	Fig sawdust activated carbon[68]	80.64	250	4.0
Garlic peel[69]	37.96	150	2.0	Sulfhydryl modified attapulgite[70]	65.79	2000	6.0
Nanostructured biosilica–calcium alginate compound[71]	33.78	200	7.0	Oak wood ash/GO/Fe_3O_4 (ref. 72)	47.16	70	6.0
Hazelnut shells[73]	18.24	70	2.5	NKF-6 zeolite[74]	45.00	—	6.0
Waste Fe^{3+}/Cr^{3+} hydroxide[75]	5.1	40	3.0	Chitosan-coated sand[39]	12.32	2000	4.5
Waste banana pith[76]	4.76	100	2.0	Polymethylmethacrylate[77]	4.79	100	—
Eucalyptus citriodora leaves biochar[78]	3.2	100	2.0	Polyethylene[77]	2.23	100	—
Rice bran-based activated carbon[50]	1.28	60	2.0	Polypropylene[77]	1.72	100	—

fits the experimental data. Also, it is argued that the value of g parameter of the R–P model can be used to confirm the adsorption behavior; if g close to zero, the adsorption is closer to Freundlich while if g close to 1 the adsorption is closer to Langmuir. Herein, the value of g is close to 1 which indicates that the adsorption behavior is closer to Langmuir. This result supports the conclusion that Langmuir model gives the best fit to the adsorption equilibrium data. The Langmuir model describe the monolayer adsorption on identical and equivalent definite localized adsorption sites. The Langmuir model include two important parameters which are the separation factor (R_L) and the theoretical monolayer saturation capacity (q_L). The value of R_L gives information about the nature of adsorption whether it is linear ($R_L = 1$), irreversible ($R_L = 0$), unfavorable ($R_L > 1$), or favorable ($0 < R_L < 1$). And the parameter q_L is commonly used to compare the efficiency of an adsorbent to others in the literature.

In this study the values of R_L were calculated according to eqn (S8)† and found to range between 0 and 1 indicating the favorability of the adsorption process. Also, Table 4 compares the value of q_L obtained in this study to those reported for the adsorption of DR31 and Pb^{2+} onto other adsorbents reported in the literature. Table 4 also includes the highest initial concentration ($C_{o,max}$) used in the isotherm study as it has been reported that the q_L significantly increases with increasing the $C_{o,max}$.[64] The value of q_L (58.13 ± 1.40) in this study was higher than those reported for the adsorption of DR31 onto several other adsorbent reported in the literature. This comparison manifests the promising potential of C1@CsNPs as adsorbent for anionic dyes.

On the other hand, analyzing the values of R^2 and error functions obtained from fitting of the studied isotherm models to the experimental data of Pb^{2+} (Table 3) discloses that R–P model has the highest R^2 and lowest error values. Thus, the experimental adsorption isotherm is best described by R–P model. The R–P model is a hybrid model that has the features of both Langmuir and Freundlich with three parameters. Thus, it is applicable for both heterogeneous and homogeneous systems that does not follow an ideal monolayer adsorption. The value of the exponent g, in this case, directs that the adsorption is closer to Freundlich. This observation matches the result that Freundlich has the second highest R^2 and lowest error values (Table 3). The value of the exponent n reflects whether the adsorption is favorable ($n > 1$), linear ($n = 1$) or unfavorable ($n < 1$). The value of n in this study indicates that the adsorption of Pb^{2+} onto C1@CsNPs is favorable. Since Langmuir model also suites the experimental data of Pb^{2+}, the value of q_L can be reliably used to compare the efficiency of C1@CsNPs to other adsorbents reported previously. The values of q_L listed in Table 4 indicate that C1@CsNPs is more efficient for Pb^{2+} adsorption than many other adsorbents and therefore it can be considered as a promising adsorbent for trace metals removal from contaminated water.

Simultaneous adsorption of DR31 and Pb^{2+}. The co-occurrence of synthetic dyes and trace metals in several industrial effluents necessitates the development and testing the ability of adsorbents for the simultaneous removal of these two groups of pollutants. Therefore, it would be meaningful to investigate the simultaneous removal of DR31 and Pb^{2+} using C1@CsNPs. Considering the precipitation of metal ions, the simultaneous removal of DR31 and Pb^{2+} was tested at pH_o 5, using 1.00 g L^{-1} of C1@CsNPs. Fig. 7 shows time profile for the amount of adsorbate per unit mass of C1@CsNPs in single and binary component systems. It can be seen from Fig. 7a and b that both DR31 and Pb^{2+} behave similarly. The amount of the adsorptive adsorbed in the binary system was slightly lower than the amount adsorbed in the unary system in the first 60 minutes. After 60 minutes the amount of adsorptive adsorbed on C1@CsNPs was equal in the unary and binary systems.

In binary systems the two adsorptives interact with each other's and this interaction result in either enhancing (synergism), reducing (antagonism) or unaffecting (non-interaction) the amount adsorbed. McKay and Al Duri[79] developed a simple model called *P*-factor (P_f, eqn (S16)†) to define the effect of the presence of two adsorptives on each other. A value of $P_f > 1$ indicates that the presence of one adsorptive promotes

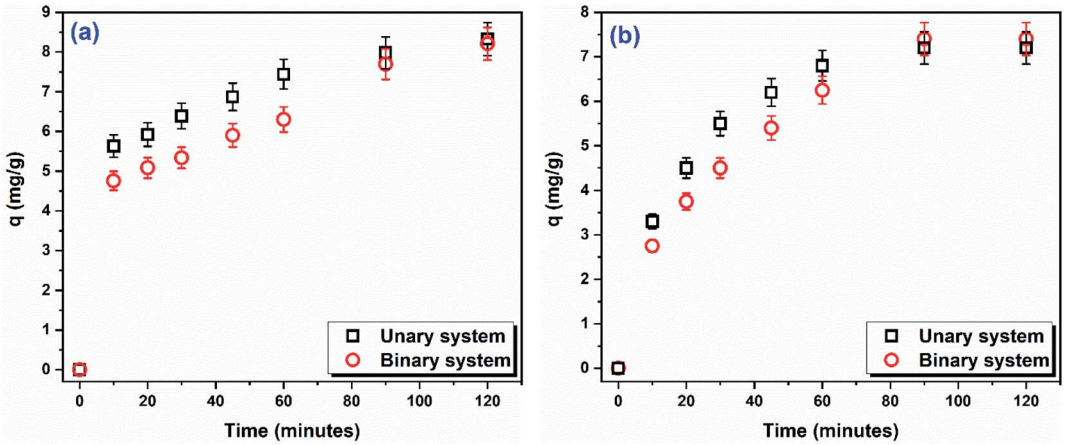

Fig. 7 Time-course of the amount of (a) DR31 and (b) Pb^{2+} adsorbed per unit mass of C1@CsNPs in unary and binary systems (C_o 10 mg L^{-1} of each of DR31 and Pb^{2+}, dosage 1.00 g L^{-1}, pH_o 5).

the adsorption of the other (synergistic effect), while a value of $P_f > 1$ indicates that the presence of an adsorptive suppresses the adsorption of the other (antagonistic effect) and a value of $P_f = 1$ indicates that the presence of the two adsorptives have no effect on the adsorption of each other's (non-interaction).

In this study, the *P*-factor was calculated and found to be 0.99 for DR31 and 1.03 for Pb^{2+}, equivalent to 1. These values indicate that the simultaneous presence of DR31 and Pb^{2+} has no effect on the adsorption of each other (non-interaction). This result implies that DR31 and Pb^{2+} do not adsorb to the same adsorption sites and that the adsorption process occurs *via* different mechanisms. This observation agrees with the results obtained for the effect of pH_o on the adsorption. As discussed above, at pH_o 5 the adsorption of DR31 is likely due to one or more of π–π stacking, dipole–dipole H-bonding, Yoshida H-bonding, n–π interactions, and anion–π interactions. While the adsorption of Pb^{2+} is likely due to electrostatic interactions and metal ion complexation. Also, the kinetic study illustrated that the adsorption of DR31 follows the PFO slightly better than the PSO while Pb^{2+} follows Elovich model. Furthermore, the isotherm study indicated that the adsorption of DR31 followed Langmuir model while Pb^{2+} followed Freundlich model. All these observations lead to the conclusion that the adsorption of DR31 and Pb^{2+} onto C1@CsNPs follows different mechanisms and do not share the same adsorption sites. Similar trend has been reported by Shikuku *et al.*,[80] who found that the presence of sulfachloropyridazine (SCP) did not affect the adsorption of sulfadimethoxine (SDM) onto iron-modified raw kaolinite clay. They concluded that SCP and SDM did not share some adsorption sites and that the adsorption process was driven by different mechanisms.

Conclusions

Simultaneously removal of synthetic dyes and trace metals from complex contaminated water is of great importance. However, these two groups of contaminants have completely different chemical, and physical properties which complicate their simultaneous removal. Herein, a new material that enables simultaneous removal of anionic dyes and cationic trace metals was successfully prepared. Thus, the designed work aimed to prepare a new coumarin derivative and entrapped into chitosan nanoparticles (CsNPs) with two different concentrations coded as C1@CsNPs and Cs@NPs. The synthesized coumarin derivative, CsNPs, C1@CsNPs and Cs@NPs were fully characterized by the means of FTIR, SEM, TEM and DLS. The prepared nanocomposites efficiently removed DR31 and Pb^{2+} in unary and binary systems. The sample C1@CsNPs achieves the highest removal of both DR31 and Pb^{2+}. In unary system, the pH_o affected remarkably the adsorption of both DR31 and Pb^{2+}, but differently. The adsorption peaked at pH_o 3.0 and 5.5 for DR31 and Pb^{2+}, respectively. The pH_o, kinetic, isotherm and binary system studies revealed that C1@CsNPs adsorbs DR31 and Pb^{2+} through different mechanisms. C1@CsNPs adsorbs DR31 through electrostatic interactions, π–π stacking, dipole–dipole H-bonding, Yoshida H-bonding, n–π interactions, and anion–π interactions. The exact mechanism depends on the pH_o. While Pb^{2+} is adsorbed onto C1@CsNPs through electrostatic interactions and complexation. The coexistence of DR31 and Pb^{2+} did not affect their adsorption. Conclusively, this work demonstrated the effectiveness, and potential of the prepared material for the simultaneous removal of anionic dyes and cationic trace metals from contaminated water.

Conflicts of interest

There are no known conflicts of interest associated with this publication and there has been no significant financial support for this work that could have influenced its outcome.

References

1 M. Benjelloun, Y. Miyah, G. Akdemir Evrendilek, F. Zerrouq and S. Lairini, *Arabian J. Chem.*, 2021, **14**, 103031.
2 P. Sherugar, M. Padaki, N. S. Naik, S. D. George and D. H. K. Murthy, *Chemosphere*, 2022, **287**, 132085.

3 C. L. Bianchi, R. Djellabi, C. Della Pina and E. Falletta, *Chemosphere*, 2022, **286**, 131941.
4 A. Abdel-Karim, M. E. El-Naggar, E. K. Radwan, I. M. Mohamed, M. Azaam and E.-R. Kenawy, *Chem. Eng. J.*, 2021, **405**, 126964.
5 T. C. Egbosiuba, M. C. Egwunyenga, J. O. Tijani, S. Mustapha, A. S. Abdulkareem, A. S. Kovo, V. Krikstolaityte, A. Veksha, M. Wagner and G. Lisak, *J. Hazard. Mater.*, 2022, **423**, 126993.
6 N. Oke and S. Mohan, *J. Hazard. Mater.*, 2022, **422**, 126864.
7 H. Xue, X. Wang, Q. Xu, F. Dhaouadi, L. Sellaoui, M. K. Seliem, A. Ben Lamine, H. Belmabrouk, A. Bajahzar, A. Bonilla-Petriciolet, Z. Li and Q. Li, *Chem. Eng. J.*, 2022, **430**, 132801.
8 M. Bergaoui, M. Khalfaoui, M. Alam, B. Guellou, M. C. Belekbir, R. Chouk, A. Erto, K. K. Yadav and Y. Benguerba, *Mater. Today Commun.*, 2022, **30**, 103056.
9 M. Pishnamazi, A. Khan, T. A. Kurniawan, H. Sanaeepur, A. B. Albadarin and R. Soltani, *J. Mol. Liq.*, 2021, **338**, 116573.
10 I. M. El-Sewify, A. Radwan, A. Shahat, M. F. El-Shahat and M. M. H. Khalil, *Microporous Mesoporous Mater.*, 2022, **329**, 111506.
11 Z. Zhang, T. Wang, H. Zhang, Y. Liu and B. Xing, *Sci. Total Environ.*, 2021, **757**, 143910.
12 J. Hong, L. Kang, X. Shi, R. Wei, X. Mai, D. Pan, N. Naik and Z. Guo, *J. Mater. Sci. Technol.*, 2022, **98**, 212–218.
13 D. D. Giri, A. Alhazmi, A. Mohammad, S. Haque, N. Srivastava, V. K. Thakur, V. K. Gupta and D. B. Pal, *Chemosphere*, 2022, **287**, 132016.
14 F. H. Margha, E. K. Radwan, M. I. Badawy and T. A. Gad-Allah, *ACS Omega*, 2020, **5**, 14625–14634.
15 H. F. Nour, R. E. Abdel Mageid, E. K. Radwan, T. A. Khattab, M. A. Olson and T. El Malah, *New J. Chem.*, 2021, **45**, 18983–18993.
16 Y. Huang, H. Zheng, X. Hu, Y. Wu, X. Tang, Q. He and S. Peng, *J. Hazard. Mater.*, 2022, **422**, 126856.
17 M. Verma, I. Lee, J. Oh, V. Kumar and H. Kim, *Chemosphere*, 2022, **287**, 132385.
18 T. N. Van, S. Debenedetti and N. De Kimpe, *Tetrahedron Lett.*, 2003, **44**, 4199–4201.
19 A. K. Chatterjee, F. D. Toste, S. D. Goldberg and R. H. Grubbs, *Pure Appl. Chem.*, 2003, **75**, 421–425.
20 C. Sproll, W. Ruge, C. Andlauer, R. Godelmann and D. W. Lachenmeier, *Food Chem.*, 2008, **109**, 462–469.
21 F. Maggi, L. Barboni, G. Caprioli, F. Papa, M. Ricciutelli, G. Sagratini and S. Vittori, *Fitoterapia*, 2011, **82**, 1215–1221.
22 T. Fotland, J. Paulsen, T. Sanner, J. Alexander and T. Husøy, *Food Chem. Toxicol.*, 2012, **50**, 903–912.
23 R. Sánchez-de-Armas, M. A. San Miguel, J. Oviedo and J. F. Sanz, *Phys. Chem. Chem. Phys.*, 2012, **14**, 225–233.
24 S. Guha, S. Lohar, A. Banerjee, A. Sahana, I. Hauli, S. K. Mukherjee, J. S. Matalobos and D. Das, *Talanta*, 2012, **91**, 18–25.
25 H. V. Chavan and B. P. Bandgar, *ACS Sustainable Chem. Eng.*, 2013, **1**, 929–936.
26 L. Pari, N. Rajarajeswari, S. Saravanan and A. Rathinam, *Biomedicine & Preventive Nutrition*, 2014, **4**, 171–176.
27 M. I. Hussain, Q. A. Syed, M. N. K. Khattak, B. Hafez, M. J. Reigosa and A. El-Keblawy, *Biologia*, 2019, **74**, 863–888.
28 J. Xu, L. Ma, D. Jiang, S. Zhu, F. Yan, Y. Xie, Z. Xie, W. Guo and X. Deng, *Food Chem.*, 2015, **187**, 75–81.
29 A. Thakur, R. Singla and V. Jaitak, *Eur. J. Med. Chem.*, 2015, **101**, 476–495.
30 L. Zhao, J. Zhang, T. Liu, H. Mou, C. Wei, D. Hu and B. Song, *J. Agric. Food Chem.*, 2019, **68**, 975–981.
31 M. Z. Hassan, H. Osman, M. A. Ali and M. J. Ahsan, *Eur. J. Med. Chem.*, 2016, **123**, 236–255.
32 D. H. Elnaggar, N. A. Abdel Hafez, H. R. Rashdan, N. A. Abdelwahed, H. M. Awad and K. A. Ali, *Mini-Rev. Med. Chem.*, 2019, **19**, 1717–1725.
33 H. Rashdan, S. M. Nasr, H. A. El-Refai and M. S. Abdel-Aziz, *J. Appl. Pharm. Sci.*, 2017, **7**, 186–196.
34 N. Nuñez-Dallos, C. Cuadrado, J. Hurtado, E. Nagles and O. García-Beltran, *Int. J. Electrochem. Sci.*, 2016, **11**, 9855–9867.
35 P. Bhaumick and L. H. Choudhury, *Polymer*, 2022, **243**, 124580.
36 R. Huang, Q. Liu, J. Huo and B. Yang, *Arabian J. Chem.*, 2017, **10**, 24–32.
37 F. Zha, S. Li and Y. Chang, *Carbohydr. Polym.*, 2008, **72**, 456–461.
38 Z. M. Ali, A. J. Laghari, A. K. Ansari and M. Y. Khuhawar, *Extraction*, 2013, **3**, 28–37.
39 M.-W. Wan, C.-C. Kan, B. D. Rogel and M. L. P. Dalida, *Carbohydr. Polym.*, 2010, **80**, 891–899.
40 P. S. Rao and R. Venkataratnam, *Tetrahedron Lett.*, 1991, **32**, 5821–5822.
41 R. J. Samuels, *J. Polym. Sci., Polym. Phys. Ed.*, 1981, **19**, 1081–1105.
42 F. L. Mi, S. S. Shyu, S. T. Lee and T. B. Wong, *J. Polym. Sci., Part B: Polym. Phys.*, 1999, **37**, 1551–1564.
43 J.-M. Yang, R.-Z. Zhang and Y.-Y. Liu, *CrystEngComm*, 2019, **21**, 5824–5833.
44 M. Mullen, N. Fontaine and W. B. Euler, *J. Fluoresc.*, 2020, **30**, 811–818.
45 N. Sakkayawong, P. Thiravetyan and W. Nakbanpote, *J. Colloid Interface Sci.*, 2005, **286**, 36–42.
46 U. Upadhyay, I. Sreedhar, S. A. Singh, C. M. Patel and K. L. Anitha, *Carbohydr. Polym.*, 2021, **251**, 117000.
47 M. J. Livani and M. Ghorbani, *Environ. Technol.*, 2018, **39**, 2977–2993.
48 Y. Safa and H. N. Bhatti, *Desalination*, 2011, **272**, 313–322.
49 H. F. Nour, T. El Malah, E. K. Radwan, R. E. Abdel Mageid, T. A. Khattab and M. A. Olson, *React. Funct. Polym.*, 2021, 104795, DOI: **10.1016/j.reactfunctpolym.2020.104795**.
50 M. Sankar, G. Sekaran, S. Sadulla and T. Ramasami, *J. Chem. Technol. Biotechnol.*, 1999, **74**, 337–344.
51 H. N. Tran, Y.-F. Wang, S.-J. You and H.-P. Chao, *Process Saf. Environ. Prot.*, 2017, **107**, 168–180.
52 S. Cheng, S. Zhao, H. Guo, B. Xing, Y. Liu, C. Zhang and M. Ma, *Bioresour. Technol.*, 2022, **343**, 126081.
53 M. M. El Bendary, E. K. Radwan and M. F. El-Shahat, *Environ. Nanotechnol., Monit. Manage.*, 2021, **15**, 100455.

54 E. K. Radwan, H. H. Abdel Ghafar, A. S. Moursy, C. H. Langford, A. H. Bedair and G. Achari, *Desalin. Water Treat.*, 2017, **80**, 297–305.
55 E. K. Radwan, M. E. El-Naggar, A. Abdel-Karim and A. R. Wassel, *Int. J. Biol. Macromol.*, 2021, **189**, 420–431.
56 S. Wang and E. Ariyanto, *J. Colloid Interface Sci.*, 2007, **314**, 25–31.
57 V. K. Gupta, B. Gupta, A. Rastogi, S. Agarwal and A. Nayak, *J. Hazard. Mater.*, 2011, **186**, 891–901.
58 R. Gong, M. Li, C. Yang, Y. Sun and J. Chen, *J. Hazard. Mater.*, 2005, **121**, 247–250.
59 A. Rajappa, K. Ramesh, V. Nandhakumar and H. Ramesh, *J. Environ. Nanotechnol.*, 2014, **3**, 43–49.
60 J. X. Lin, S. L. Zhan, M. H. Fang and X. Q. Qian, *J. Porous Mater.*, 2007, **14**, 449–455.
61 E. K. Radwan, H. Kafafy, S. T. El-Wakeel, T. I. Shaheen, T. A. Gad-Allah, A. S. El-Kalliny and M. E. El-Naggar, *Cellulose*, 2018, **25**, 6645–6660.
62 C. Tejada, A. Herrera and E. Ruiz, *Ing. Compet.*, 2016, **18**, 117–127.
63 A. N. Ebelegi, N. Ayawei and D. Wankasi, *Open J. Phys. Chem.*, 2020, **10**, 166.
64 Y. Li, Q. Li, C. Wu, X. Luo, X. Yu and M. Chen, *Sci. Total Environ.*, 2020, **699**, 134222.
65 T. I. Shaheen, E. K. Radwan and S. T. El-Wakeel, *Microporous Mesoporous Mater.*, 2022, **338**, 111996.
66 N. M. Mahmoodi, J. Abdi and D. Bastani, *J. Environ. Health Sci. Eng.*, 2014, **12**, 96.
67 K. Karthick, C. Namasivayam and L. A. Pragasan, *Indian J. Chem. Technol.*, 2017, **24**, 73–81.
68 M. Ghasemi, M. Naushad, N. Ghasemi and Y. Khosravi-Fard, *J. Ind. Eng. Chem.*, 2014, **20**, 454–461.
69 A. Asfaram, M. R. Fathi, S. Khodadoust and M. Naraki, *Spectrochim. Acta, Part A*, 2014, **127**, 415–421.
70 C. Fu, X. Zhu, X. Dong, P. Zhao and Z. Wang, *Arabian J. Chem.*, 2021, **14**, 102960.
71 R. Darvishi Cheshmeh Soltani, A. Khataee and A. Koolivand, *Environ. Prog. Sustainable Energy*, 2015, **34**, 1435–1443.
72 R. Pelalak, Z. Heidari, S. M. Khatami, T. A. Kurniawan, A. Marjani and S. Shirazian, *Arabian J. Chem.*, 2021, **14**, 102991.
73 M. Fathi and A. Asfaram, *J. Chem. Health Risks*, 2011, **1**, 1–12.
74 L. Gao, Z. Li, W. Yi, Y. Li, P. Zhang, A. Zhang and L. Wang, *J. Environ. Chem. Eng.*, 2021, **9**, 105602.
75 C. Namasivayam and S. Sumithra, *J. Environ. Manage.*, 2005, **74**, 207–215.
76 C. Namasivayam and N. Kanchana, *Chemosphere*, 1992, **25**, 1691–1705.
77 M. Shen, B. Song, G. Zeng, Y. Zhang, F. Teng and C. Zhou, *Chem. Eng. J.*, 2021, **405**, 126989.
78 R. T. Kapoor and S. Sivamani, *Biomass Convers. Biorefin.*, 2021, DOI: **10.1007/s13399-021-01681-w**.
79 G. McKay and B. Al Duri, *Chem. Eng. Process.*, 1987, **22**, 145–156.
80 V. O. Shikuku, R. Zanella, C. O. Kowenje, F. F. Donato, N. M. G. Bandeira and O. D. Prestes, *Appl. Water Sci.*, 2018, **8**, 175.